

# High Performance P<sup>3</sup>M N-body code: CUBEP3M

Joachim Harnois-Déraps<sup>1,2</sup> <sup>★</sup>, Ue-Li Pen<sup>1</sup>, Ilian T. Iliev<sup>3</sup>, Hugh Merz<sup>4</sup>,  
 JD Emberson<sup>1,5</sup> and Vincent Desjacques<sup>6,7</sup>

<sup>1</sup>Canadian Institute for Theoretical Astrophysics, University of Toronto, M5S 3H8, Ontario, Canada

<sup>2</sup>Department of Physics, University of Toronto, M5S 1A7, Ontario, Canada

<sup>3</sup>Astronomy Centre, Department of Physics and Astronomy, Pevenssey II Building, University of Sussex, BN1 9QH, Brighton, United Kingdom

<sup>4</sup>SHARCNET, Laurentian University, P3E 2C6, Ontario, Canada

<sup>5</sup>Department of Astronomy and Astrophysics, University of Toronto, M5S 3H4, Ontario, Canada

<sup>6</sup>Institute for Theoretical Physics, University of Zürich, Zürich, CH 8057, Switzerland

<sup>7</sup>Université de Genève and Center for Astroparticle Physics, 24 Quai Ernest Ansermet, 1211 Genève 4, Switzerland

8 June 2012

## ABSTRACT

This paper presents CUBEP3M, an upgraded version of PMFAST that is now one of the fastest highest performance public N-body code. Gravity is solved on a two-level mesh with sub-grid precision due to the particle-particle (pp) interactions inside and across neighboring cells. Among important improvements, CUBEP3M has a volumetric decomposition, allowing for a massive parallelization over more than 20,000 cores, and has achieved close to ideal weak scaling even at this scale. In addition, force kernels have been improved for enhanced matching of the two mesh contributions near the cutoff length, and the code is now equipped with a unique particle identification tag system that allows reconstruction of individual particle trajectories between time steps. In parallel, many utilities and extensions have been added to the standard code package, including a runtime halo finder, a tunable range for the exact pp force, a non-Gaussian initial conditions generator, etc. We discuss the structure, the accuracy, any known systematic effects, and the scaling performance of the code and its utilities, when applicable.

**Key words:** N-body simulations — Large scale structure of Universe — Dark matter

## 1 INTRODUCTION

Many physical and astrophysical systems are subject to non-linear dynamics and rely on N-body simulations to describe the evolution of bodies. One of the main field of application is the modelling of large scale structures, which are driven by the sole force of gravity. Recent observations of the cosmic microwave background (Komatsu et al. 2009, 2011), of galaxy clustering (York et al. 2000; Colless et al. 2003; Schlegel et al. 2009; Drinkwater et al. 2010) of weak gravitational lensing (Heymans & CFHTLenS Collaboration 2012; Sheldon et al. 2009) and of supernovae redshift-distance relations all point towards a standard model of cosmology, in which dark energy and collision-less dark matter occupy more than 95 per cent of the total energy density of the universe. In such a paradigm, pure N-body code are perfectly suited to describe the dynamics, as long as baryonic physics is not very important, or at least we understand how the baryonic fluid feeds back on the dark matter structure. The next generation of measurements aim at constraining the cosmological parameters at the per cent level, and the theoreti-

cal understanding of the non-linear dynamics that govern structure formation heavily relies on numerical simulations.

For instance, a measurement of the baryonic acoustic oscillation (BAO) dilation scale can provide tight constraints on the dark energy equation of state (Eisenstein et al. 2005; Tegmark et al. 2006; Percival et al. 2007; Schlegel et al. 2009). The most optimal estimates of the uncertainty requires the knowledge of the matter power spectrum covariance matrix, which is only accurate when measured from a large sample of N-body simulations (Rimes & Hamilton 2005; Takahashi et al. 2009, 2011). For the same reasons, the most accurate estimates of weak gravitational lensing signal is obtained by propagating photons in past light cones that are extracted from simulated density fields (Vale & White 2003; Sato et al. 2009; Hilbert et al. 2009). Another area where large-scale N-body simulations have in recent years been instrumental are in simulations of early cosmic structures and reionization (e.g. Iliev et al. 2006; Zahn et al. 2007; Trac & Cen 2007; Iliev et al. 2011). The reionization process is primarily driven by low-mass galaxies, which for both observational and theoretical reasons, need to be resolved in fairly large volumes, which demands simulations with a very large dynamic range.

<sup>★</sup> E-mail: jharno@cita.utoronto.ca

The basic problem that is addressed with N-body codes is the

time evolution of an ensemble of  $N$  particles that is subject to gravitational attraction. The brute force calculation requires  $O(N^2)$  operations, a cost that exceeds the memory and speed of current machines for large problems. Solving the problem on a mesh (Hockney & Eastwood 1981) reduces to  $O(N \log N)$  the number of operations, as it is possible to solve for the particle-mesh (PM) interaction with fast Fourier transforms techniques with high performance libraries such as FFTW (Frigo & Johnson 2005).

With the advent of large computing facilities, parallel computations have now become common practice, and N-body codes have evolved both in performance and complexity. Many have opted for ‘tree’ algorithms, including GADGET (Springel et al. 2001; Springel 2005), PMT (Xu 1995), GOTPM (Dubinski et al. 2004), and Hydra (Couchman et al. 1995), in which the local resolution increases with the density of the matter field. These often have the advantage to balance the work load across the computing units, which enable fast calculations even in high density regions. The drawback is a significant loss in speed, which can be only partly recovered by turning off the tree algorithm. The same reasoning applies to mesh-refined codes (Couchman 1991), which in the end are not designed to perform fast PM calculations on large scales.

PMFAST (Merz et al. (2005), MPT hereafter) is one of the first code designed specifically to optimize the PM algorithm, both in terms of speed and memory usage. It uses a two-level mesh algorithm based on the gravity solver of Trac & Pen (2003). The long range gravitational force is computed on a grid four times coarser, such as to minimize the MPI communication time and to fit in system’s memory. The short range is computed locally on a finer mesh, and only the local sub-volume needs to be stored at a given time, allowing for OPENMP parallel computation. This this setup enable the code to evolve large cosmological systems both rapidly and accurately, on relatively modest clusters. One of the main advantage of PMFAST over other PM codes is that the number of large arrays is minimized, and the global MPI communications are cut down to the minimum: for passing particle at the beginning of each time step, and for computing the long range FFTs. As described in MPT, access to particles is accelerated with the use of linked lists, deletion of ‘ghost’ particles in buffer zones is done at the same time as particles are passed to adjacent nodes, and the global FFTs are performed with a slab decomposition of the volumes via a special file transfer interface, designed specifically to preserve a high processor load.

Since its first published version, PMFAST has evolved in many aspects. The first major improvement was to transform the volume decomposition in multi-node configurations from slabs to cubes. The problem with slabs is that they do not scale well to large runs: as the number of cells per dimension increases, the thickness of each slab shrinks rapidly, until it reaches the hard limit of a single cell layer. With this enhancement, the code name was changed to CUBEPM. Soon after, it incorporated particle-particle (pp) interactions at the sub-grid level, and was finally renamed CUBEP3M. The public package now includes a significant number of new features: the pp force can be extended to an arbitrary range, the size of the redshift jumps can be constrained for improved accuracy during the first time steps, a runtime halo finder has been implemented, the expansion has also been generalized to include a redshift dependent equation of state of dark energy, there is a system of unique particle identification that can be switched on or off, and the initial condition generator has been generalized as to include non-Gaussian features. PMFAST was equipped with a multi-time stepping option that has not been tested on CUBEP3M yet, but which is, in principle at least, still available. It also contains support for gas cosmological

evolution through a TVD MHD module, and a coupling interface with the radiative transfer code C2-Ray (Mellema et al. 2006).

CUBEP3M is one of the most competitive public N-body code and has been involved in a number of scientific applications over the last few years, spanning the field of weak lensing (Vafaei et al. 2010; Lu & Pen 2008; Doré et al. 2009; Lu et al. 2010; Yu et al. 2010; Harnois-Déraps et al. 2012), BAO (Zhang et al. 2010; Ngan et al. 2011; Harnois-Déraps & Pen 2011; Harnois-Déraps et al. 2012), formation of early cosmic structures (Iliev et al. 2008, 2010), observations of dark stars (Zackrisson et al. 2010; Ilie et al. 2012) and reionization (Iliev et al. 2011; Fernandez et al. 2011; Friedrich et al. 2011; Mao et al. 2012; Datta et al. 2011; Friedrich et al. 2012). It is thus important for the community to have access to a paper that describes the methodology, the accuracy and the performance of this public code.

Since CUBEP3M is not new, the existing accuracy and systematic tests were performed by different groups, on different machines, and with different geometric and parallelization configurations. It is not an ideal situation in which to quantify the performance, and each test must be viewed as a separate measurement that quantifies a specific aspect of the code. We have tried to keep to a minimum the number of such different runs, and although the detailed numbers vary with the problem size and the machines, the general trends are rather universal.

Tests on constraints of the redshift step size were performed on the Sunnyvale beowulf cluster at the Canadian Institute for Theoretical Astrophysics (CITA). Each node contains 2 Quad Core Intel(R) Xeon(R) E5310 1.60GHz processors, 4GB of RAM, a 40 GB disk and 2 gigE network interfaces. We generate a set of Gaussian initial conditions at a starting redshift of  $z = 100$ , with a box size equal to  $200h^{-1}\text{Mpc}$ , we placed  $256^3$  particles on a grid with  $2^3$  more cells, and let them evolve until  $z = 0$ . Tests on improvements of the force calculations were performed on the same machine, but with a box size of  $500h^{-1}\text{Mpc}$ . Hereafter we refer to these simulation sets as the CITA256 configurations, and specify which volume was used in each context.

For tests of the code accuracy, of the non-Gaussian initial conditions generator and of the run time halo finder algorithm, we used a third simulation configuration series that was run at the Texas Advanced Computing Centre (TACC) on Ranger, a Sun-Blade x6420 system with AMD x86\_64 Opteron Quad Core 2.3 GHz ‘Barcelona’ processors and Infiniband networking. These RANGER4000 simulations evolved  $4000^3$  particles from  $z = 100$  to  $z = 0$  with a box side of  $3.2h^{-1}\text{Gpc}$  on 4000 cores.

The paper is structured as follow: section 2 reviews the structure and flow of the main code; section 3 describes how Poisson equation is solved on the two-mesh system; we then present in section 4 the scaling of the code to very large problems, including much larger runs that were produced at various high performance computing centers; section 5 discuss the accuracy and systematic effects of the code. We then describe in section 6 the run-time halo finder, in section 7 various extensions to the default configuration, and conclude afterwards.

## 2 REVIEW OF THE CODE STRUCTURE

An optimal large scale N-body code must address many challenges: minimize the memory footprint to allow larger dynamical range, minimize the passing of information across computing nodes, reduce and accelerate the memory accesses to the large scale arrays, make efficient use of high performance libraries to speed up stan-

dard calculations like Fourier transforms, just to name a few. In the realm of parallel programming, high efficiency can be assessed when a high load is balanced across all processors most of the time. In this section, we present the general strategies adopted to address these challenges<sup>1</sup>. We start with a walkthrough the code flow, and briefly discuss some specific sections that depart from standard N-body codes, while referring the reader to future sections for detailed discussions on selected topics.

As mentioned in the Introduction section, CUBEP3M is a FORTRAN90 N-body code that solves Poisson's equation on a two-level mesh, with sub-cell accuracy thanks to particle-particle interactions. The code has extensions that departs from this basic scheme, and we shall come back to these later, but for the moment, we adopt the standard configuration. The long range component of the gravity force is solved on the coarse grid, and is global in the sense that the calculations require knowledge about the full simulated volume. The short range force and the particle-particle interactions are computed in parallel on a second level of cubical decomposition of the local volumes, the *tiles*. To make this possible, the fine grid arrays are constructed such as to support parallel memory access. In practice, this is done by adding an additional dimension to the relevant arrays, such that each CPU accesses a unique memory location. The force matching between the two meshes is performed by introducing a cutoff length,  $r_c$ , in the definition of the two force kernels. The value of  $r_c = 16$  fine cells was found to balance the communication overhead between processes and the accuracy of the match between the two meshes.

The computation of the short range force requires each tile to store the fine grid density of a region that includes a buffer surface around the physical volume it is assigned. The thickness of this surface must be larger than  $r_c$ , and we find that a 24 cells deep buffer is a good compromise between memory usage and accuracy. This is basically to fully compensate for the coarse mesh calculations, whose CIC interpolation scheme reaches two coarse cells deep beyond the cutoff.

When it comes to finding haloes at run time, this buffer can create a problem, because a large object located close to the boundary can have a radius larger than the buffer zone, in which case it would be truncated and be assigned a wrong mass, center of mass, etc. It could then be desirable to increase the buffer zone around each tile, at the cost of a loss of memory dedicated to the actual physical volume, and the code is designed to allow for such a flexibility.

Because the coarse grid arrays require  $4^3$  times less memory per node, it does not contribute much to the total memory requirement, and the bulk of the foot-print is concentrated in a handful of fine grid arrays. Some of these are only required for intermediate steps of the calculations, hence it is possible to hide therein many coarse grid arrays<sup>2</sup>. We present here the largest arrays used by the code:

- (i) `xv` stores the position and velocity of each particle
- (ii) `ll` stores the linked-list that accelerate the access to particles in each coarse grid cell
- (iii) `rho_f` and `cmplx_rho_f` store the local fine grid density in real and Fourier space respectively

<sup>1</sup> Many originate directly from MPT and were preserved in CUBEP3M; those will be briefly mentioned, and we shall refer the reader to the original PMFAST paper for greater details.

<sup>2</sup> This memory recycling is done with ‘equivalence’ statements in F90

```
program cubep3m
  call initialize
  do
    call timestep
    call particle_mesh
    if(checkpoint_step) then
      call checkpoint
    elseif(last_step)
      exit
    endif
  enddo
  call finalize
end program cubep3m
```

**Figure 1.** Overall structure of the code simplified for readability.

- (iv) `force_f` stores the force of gravity (short range only) along the three Cartesian directions
- (v) `kern_f` stores the fine grid force kernel in the three directions
- (vi) `PID` stores the unique particle identification tags.

The particle ID is a feature that can be switched off by removing a compilation flag, and allows to optimize the code for higher resolution configurations.

The code flow is presented in Fig. 1 and 2. Before entering the main loop, the code starts with an initialization stage, in which many declared variables are assigned default values, the redshift checkpoints are read, the FFTW plans are created, and the MPI communicators are defined. The phase-space array is obtained from the output of the initial conditions generator, and the force kernels on both grids are constructed from the specific geometry of the simulation. For clarity, all these operations are collected under the subroutine `call initialize` in Fig. 1, although they are actually distinct calls in the code.

Each iteration of the main loop starts with the `timestep` subroutine, which proceeds to a determination of the redshift jump by comparing the step size constraints from each force components and from the scale factor. The cosmic expansion is found by Taylor expanding Friedmann's equation up to the third order in the scale factor, and can accommodate constant or running equation of state of dark energy. The force of gravity is then solved in the `particle_mesh` subroutine, which first updates the positions and velocities of the dark matter particles, exchange with neighbouring nodes those that have exited to volume, creates a new linked list, then solve Poisson's equation. This subroutine is conceptually identical to that of PMFAST, with the exception that CUBEP3M decomposes the volume into cubes (as opposed to slabs). The loop over tiles and the particle exchange are thus performed in three dimensions. When the short range and pp forces have been calculated on all tiles, the code exits the parallel OPENMP loop and proceeds to the long range. This section of the code is also parallelized on many occasions, but, unfortunately, the current MPI-FFTW do not allow multi-threading. There is thus an inevitable loss of efficiency during each global Fourier transforms, during which only the single core MPI process is active<sup>3</sup>. As in PMFAST, the particle position and velocity updates are performed in a leap frog scheme (Hockney & Eastwood 1981).

<sup>3</sup> Other libraries such as P3DFFT (<http://code.google.com/p/p3dff/>) currently permit an extra level of parallelization, and it is our plan to migrate to one of these in the near future.

```

subroutine particle_mesh
  call update_position + apply random offset
  call link_list
  call particle_pass
  !$omp parallel do
  do tile = 1, tiles_node
    call rho_f_ngp
    call cmplx_rho_f
    call kernel_multiply_f
    call force_f
    call update_velocity_f
    if(pp = .true.) then
      call link_list_pp
      call force_pp
      call update_velocity_pp
      if(extended_pp = .true.) then
        call link_list_pp_extended
        call force_pp_extended
        call update_velocity_pp_extended
      endif
    endif
  end do
  !$omp end parallel do
  call rho_c_ngp
  call cmplx_rho_c
  call kernel_multiply_c
  call force_c
  call update_velocity_c
  delete_buffers
end subroutine particle_mesh

```

**Figure 2.** Overall structure of the two-level mesh algorithm. We have included the section that concerns the standard pp and the extended pp force calculation, to illustrate that they follows similar linked-list logic.

If the current redshift corresponds to one of the checkpoints, the code advances all particles to their final location and writes them to file. Similarly, the code can compute two-dimensional projections of the density field, halo catalogues (see section 6 for details), and can compute the power spectrum on the coarse grid at run time. The code exits the loop when it has reached the final redshift, it then wraps up the FFTW plans and clears the MPI communicators. We have collected those operations under the subroutine `finalize` for concision.

Other considerations that need to be considered is that any decomposition geometry somehow limits permissible grid sizes, and that volume evenly decomposed into cubic sub-sections – such as CUBEP3M – requires the number of MPI processes to be a perfect cube. Also, since the decomposition is volumetric, as opposed to density dependent – it suffers from load imbalance when probing deep into the non-linear regime.

### 3 POISSON SOLVER

This section reviews how Poisson’s equation is solved on a double-mesh configuration. Many parts of the algorithm are identical to PMFAST, hence we refer the reader to section 2 of MPT for more details. In CUBEP3M, the mass default assignment scheme are a ‘cloud-in-cell’ (CIC) interpolation for the coarse grid, and a ‘nearest-grid-point’ (NGP) interpolation for the fine grid (Hockney & Eastwood 1981). This choice is motivated by the fact that the most straightforward way to implement a P<sup>3</sup>M algorithm on a mesh is to have exactly zero mesh force inside a grid, which is only true for the NGP interpolation. Although CIC generally has a smoother

and more accurate force, the pp implementation enhances the code resolution by almost an order of magnitude. We impose a softening length of one tenth of a grid cell to prevent large scattering; particles separated by less than this distance have their particle-particle force set to zero.

The code units inherit from (Trac & Pen 2004) and are summarized here for completeness. The comoving length of a fine grid cell is set to one, such that the unit length in simulation unit is

$$1\mathcal{L} = a \frac{L}{N} \quad (1)$$

where  $a$  is the scale factor,  $N$  is the total number of cells along one dimension, and  $L$  is the comoving volume in  $h^{-1}\text{Mpc}$ . The mean comoving mass density is also set to unity in simulation units, which, in physical units, corresponds to

$$1\mathcal{D} = \rho_m(0)a^{-3} = \Omega_m \rho_c a^{-3} = \frac{3\Omega_m H_o^2}{8\pi G a^3} \quad (2)$$

$\Omega_m$  is the matter density,  $H_o$  is the Hubble’s constant,  $\rho_c$  is the critical density today, and  $G$  is Newton’s constant. The mass unit is found with  $\mathcal{M} = \mathcal{D}\mathcal{L}^3$ . Specifying the value of  $G$  on the grid fixes the time unit, and with  $G_{grid} = 1/(6\pi a)$ , we get:

$$1\mathcal{T} = \frac{2a^2}{3} \frac{1}{\sqrt{\Omega_m H_o^2}} \quad (3)$$

These choices completely determine the conversion between physical and simulation units. For instance, the velocity units are given by  $1\mathcal{V} = \mathcal{L}/\mathcal{T}$ .

The force of gravity on a mesh can be computed either with a gravitational potential kernel  $\omega_\phi(\mathbf{x})$  or a force kernel  $\omega_F(\mathbf{x})$ . Gravity fields are curl-free, which allows us to relate the potential  $\phi(\mathbf{x})$  to the source term via Poisson’s equation:

$$\nabla^2 \phi(\mathbf{x}) = 4\pi G \rho(\mathbf{x}) \quad (4)$$

We solve this equation in Fourier space, where we write:

$$\tilde{\phi}(\mathbf{k}) = \frac{-4\pi G \tilde{\rho}(\mathbf{k})}{k^2} \equiv \tilde{\omega}_\phi(\mathbf{k}) \tilde{\rho}(\mathbf{k}) \quad (5)$$

The potential in real space is then obtained with an inverse Fourier transform, and the kernel becomes  $\omega_\phi(\mathbf{x}) = -G/r$ . Using the convolution theorem, we can write

$$\phi(\mathbf{x}) = \int \rho(\mathbf{x}') \omega_\phi(\mathbf{x}' - \mathbf{x}) d\mathbf{x}' \quad (6)$$

and

$$\mathbf{F}(\mathbf{x}) = -m \nabla \phi(\mathbf{x}) \quad (7)$$

Although this approach is fast, it involves a finite differentiation at the final step, which enhances the numerical noise. We therefore opt for a force kernel, which is more accurate, even though it requires four extra Fourier transforms. In this case, we must solve the convolution in three dimensions and define the force kernel  $\omega_F$  such as:

$$\mathbf{F}(\mathbf{x}) = \int \rho(\mathbf{x}') \omega_F(\mathbf{x}' - \mathbf{x}) d\mathbf{x}' \quad (8)$$

Because the gradient acting on  $\mathbf{F}$  affects only un-prime variables, we can express the force kernel as a gradient of the potential kernel. Namely:

$$\omega_F(\mathbf{x}) \equiv -\nabla \omega_\phi(\mathbf{x}) = -\frac{mG\hat{\mathbf{r}}}{r^2} \quad (9)$$

Following the spherically symmetric matching technique of MPT (section 2.1), we split the force kernel into two components,

for the short and long range respectively, and match the overlapping region with a polynomial. Namely, we have:

$$\omega_s(r) = \begin{cases} \omega_F(r) - \beta(r) & \text{if } r \leq r_c \\ 0 & \text{otherwise} \end{cases} \quad (10)$$

and

$$\omega_l(r) = \begin{cases} \beta(r) & \text{if } r \leq r_c \\ \omega_F(r) & \text{otherwise} \end{cases} \quad (11)$$

The vector  $\beta(r)$  is related to the fourth order polynomial that is used in the potential case described in MPT by  $\beta = -\nabla\alpha(r)$ . The coefficients are found by matching the boundary conditions at  $r_c$  up to the second derivative, and we get

$$\beta(r) = \left[ -\frac{7r}{4r_c^3} + \frac{3r^3}{4r^5} \right] \hat{\mathbf{r}} \quad (12)$$

Because these calculations are performed on two grids of different resolution, a sampling window function must be convoluted both with the density and the kernel (see [Eq. 7-8] of MPT). When matching the two force kernels, the long range force is always on the low side close to the cutoff region, whereas the short range force is uniformly scattered across the theoretical  $1/r^2$  value – intrinsic features of the CIC and NGP interpolation schemes respectively. By performing force measurements on two particles randomly placed in the volume, we identified a small region surrounding the cutoff length in which we empirically adjust both kernels such as to improve the match. Namely, for  $14 \leq r \leq 16$ ,  $\omega_s(r) \rightarrow 0.985\omega_s(r)$ , and for  $12 \leq r \leq 16$ ,  $\omega_l(r) \rightarrow 1.2\omega_l(r)$ .

As mentioned in section 2 and summarized in Fig. 2, the force kernels are first in the code initialization stage. Eq. 8 is then solved with fast Fourier transform along each directions, and is applied onto particles in the update\_velocity subroutine.

As an option, PMFAST could run with a different set of kernels, described in MPT as the ‘least square matching’, which basically adjust the kernels on cell-by-cell basis based on minimization of the deviation with respect to the Newtonian predictions. This was originally computed such as to optimize the force calculation for the case where both grids are obtained from CIC interpolation. Moving to a mix CIC/NGP scheme requires solving the system of equations with the new configuration, a straightforward operation. (**results are presented somewhere?**)

Finally, a choice must be done concerning the longest range of the coarse mesh force. Gravity can be either a) an accurate  $1/r^2$  force, as far as the volume allows, or b) modified to correctly match the periodicity of the boundary conditions. By default, the code is configured along to the second choice, which accurately models the growth of structures at very large scales. However, detailed studies of gravitational collapse of a single large object would benefit from the first settings, even though the code is not optimal for such settings.

#### 4 SCALING PERFORMANCES

The parallel algorithm of CUBEP3M is designed for ‘weak’ scaling, i.e. if the number of cores and the problem size increase in proportion to each other, then for ideal scaling the wall-clock time should remain the same. This is to be contrasted with ‘strong’ scaling codes, whereby the same problem solved on more cores should take proportionately less wall-clock time. This weak scaling requirement is dictated by the problems we are typically investigating (very large and computationally-intensive) and our goals,

which are to address such large problems in the most efficient way, rather than for the least wall-clock time. Furthermore, we recall that there is no explicit load balancing feature, thus the code is maximally efficient when the sub-domains contain roughly an number of particles. This is true for most cosmological-size volumes that do not resolve too deep in the non-linear regime, but not for e.g. simulations of a single highly-resolved galaxy.

Because of the volumetric decomposition, the total number of MPI processes needs to be a perfect cube. Also, for maximal resource usage, the number of tiles per node should be a multiple of the number of available CPUs per MPI process, such that no core sits idle in the threaded block. Given the available freedom in the parallel configuration, as long as the load is balanced, it is generally good practice to maximize the number of OPENMP threads and minimize the number of MPI processes: the information exchange between cores that are part of the same motherboard is generally much faster. In addition, having fewer MPI processes reduces the total amount of buffer zones, freeing memory that can be used to increase the mesh resolution. As one probes deeper into the non-linear regime however, the formation of dense objects can cause memory problems in such configurations, and increasing the number of MPI processes helps to ensure memory locality, especially in non-uniform memory access (NUMA) environments.

The intermediary version of the code – CUBEP3M – was first ported to the IBM Blue Gene/L platform, and achieved weak-scaling up to 4096 processes (over a billion particles), with the N-body calculation only incurring a 10 per cent overhead at runtime (compared to 8 processes) for a balanced workload (**How do we cite Hugh’s work on blue gene?**). In order to accommodate the limited amount of memory available per processing core on the Blue Gene/L platform machines, it was necessary to perform the long range MPI FFT with a volumetric decomposition ( Eleftheriou et al. 2005). Slab decomposition would have required a volume too large to fit in system memory given the constraints in the simulation geometry.

The scaling of CUBEP3M was first tested with a dedicated series of simulations – the CURIE simulation suite– by increasing the size and number of cores on the ‘fat’ (i.e. large-memory) nodes of the Curie supercomputer at the Très Grand Centre de Calcul (TGCC) in France. For appropriate direct comparison, all these simulations were performed using the same particle mass ( $M_{\text{particle}} = 1.07 \times 10^{11} M_\odot$ ) and force resolution (softening length  $50 h^{-1}\text{kpc}$ ). The box sizes used range from  $256 h^{-1}\text{Mpc}$  to  $2048 h^{-1}\text{Mpc}$ , and the number of particles from  $256^3$  to  $2048^3$ . Simulations were run on 32 up to 2048 computing cores, also starting from redshift  $z = 100$ , and evolving until  $z = 0$ . Our results are shown in Fig. 3 and in Table 1, and present excellent scaling, within  $\sim 3$  per cent of ideal, at least for up to 2048 cores.

We have also ran CUBEP3M on a much larger number of cores, from 8000 to up to 21,976, with  $5488^3$ - $6000^3$  (165 to 216 billion) particles on Ranger and on JUROPA at the Jülich Supercomputing Centre in Germany, which is an Intel Xeon X5570 (Nehalem-EP) quad-core 2.93 GHz system, also interconnected with Infiniband. Since it is not practical to perform dedicated scaling tests on such a large number of computing cores, we instead list in Table 2 the data directly extracted from production runs. We have found the code to scale within 1.5 per cent of ideal up to 4096 cores. For larger sizes ( $\geq 10,976$  cores), the scaling is less ideal, due to increased communication costs, I/O overheads (a single timeslice of  $5488^3$  particles is 3.6 TB) and load balancing issues, but still within  $\sim 20$

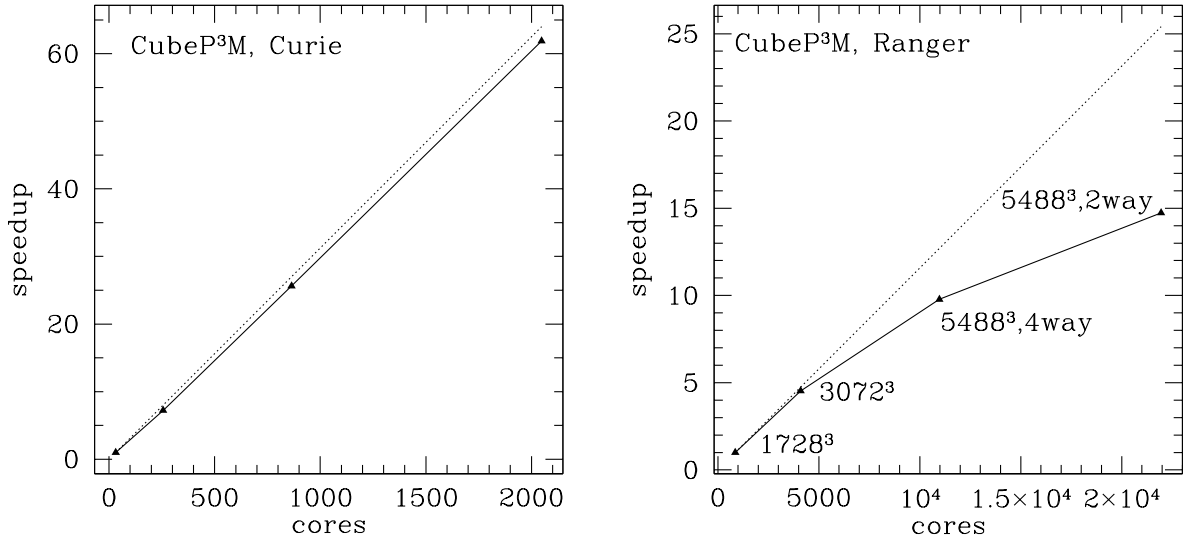


**Figure 3.** Scaling of CUBEP3M on Curie fat nodes (left) and on Ranger TACC facility for very large number of cores (right). Plotted is the code speedup ( $N_{\text{particles}}^3/t_{\text{wallclock}}$ ) against core count, normalized by the smallest run in each case. Dashed line indicates the ideal weak scaling. The data are listed in Table 1.

**Table 1.** Scaling of CUBEP3M on Curie. Speedup is scaled to the smallest run.

number of cores	speedup	ideal speedup	absolute timing (min)	$N_{\text{particles}}$	box size ( $h^{-1}\text{Mpc}$ )
32	1.00	-	3.2	$256^3$	256
256	7.21	8	3.55	$512^3$	512
864	25.63	27	4.8	$864^3$	864
2048	61.87	64	26.48	$2048^3$	2048

**Table 2.** Scaling of CUBEP3M on Ranger. Speedup is scaled to the smallest run.

number of cores	speedup	ideal speedup	absolute timing (min)	$N_{\text{particles}}$	box size ( $h^{-1}\text{Mpc}$ )
864	1.00	-	258	$1728^3$	6.3
4096	4.53	4.74	320	$3072^3$	11.4
10976	9.78	12.7	845	$5488^3$	20
21952	14.73	25.4	561	$5488^3$	20

per cent of ideal. These first three Ranger runs were performed with 4 MPI processes and 4 threads per Ranger node ('4way')<sup>4</sup>.

Furthermore, due to the increasing clustering of structures at those small scales, some of the cuboid sub-domains came to contain a number of particles well above the average, thereby requiring more memory per MPI process in order to run until the end. As a consequence, *throughout most of the evolution(Ilian, did you actually restarted simulations and switched 4ways to 2ways?)* the largest two of these simulations were run with 4096 and 21,952 cores and with only 2 MPI processes and 8 threads per Ranger node ('2way'), which on Ranger allows using up to 16 GB of RAM per MPI process<sup>5</sup>. Because each processor accesses memory that is not

<sup>4</sup> For these very large runs, we used a NUMA script *tacc\_affinity*, specially-provided by the technical staff, that bind the memory usage to local sockets, thus ensuring memory affinity. This becomes important because the memory sockets per node (32 GB RAM/node on Ranger) are actually not equal-access. Generally, the local memory of each processor has much shorter access time.

<sup>5</sup> In order to insure local memory affinity, a second special NUMA control

fully local, this configuration does affect the performance somewhat, as does the imperfect load balancing that arises in such situations. This can be seen in the rightmost point of Fig. 3 (right panel), where the scaling 42 per cent below the ideal. We note that we still get  $\sim 1.5$  speedup from doubling the core count, even given these issues. Overall the code scaling performance is thus satisfactory even at extremely large number of cores. We expect the code to handle even larger problems efficiently, and is thus well suited to run on next generation Petascale systems.

Finally, we note that several special fixes had to be developed by the TACC and JUROPA technical staff in order for our largest runs to work properly. In particular, we encountered unexpected problems from software libraries such as MPICH and FFTW when applied to calculations of such unprecedented size.

**(We should also compare the memory usage to other codes like Gadget. Ilian mentioned Gadget uses 90 Bytes per parti-**

script, *tacc\_affinity\_2way*) was developed for us by the TACC technical staff and allowed to run more efficiently in this mode.

cle. Is cubep3m really using 130 Bytes per particle? Check with `mem_usage`.)

## 5 ACCURACY AND SYSTEMATICS

This section describes the systematics effects that are inherent to our  $P^3M$  algorithm. We start with a demonstration of the accuracy with a power spectrum measurement of a RANGER4000 simulation. The halo mass function also assess the code capacity to model gravitational collapse, but depends on the particular halo finder used, which we discuss in section 6. For the moment, we focus on the two-point function, and further quantify the accuracy of the force calculation with comparisons to Newton's law of gravitation.

### 5.1 Power Spectrum

One of the most reliable way to assess the simulation's accuracy at evolving particles is to measure the density power spectrum at late time, and compare to non-linear prediction. For an over-density field  $\delta(x)$ , the power spectrum is extracted from the two point function in Fourier space as:

$$\langle |\delta(k)\delta(k')| \rangle = (2\pi)^3 P(k)\delta_D(k' - k) \quad (13)$$

where the angle bracket corresponds to an ensemble (or volume) average. We plot in Fig. 4 the dimensionless power spectrum in a RANGER4000 simulation and observe that the agreement with the non-linear prediction of Lewis et al. (2000) is at the per cent level over a large dynamical range. The drop of power at high- $k$  is caused by the finite resolution, and the fluctuations at low- $k$  are caused by the white noise imposed in the initial conditions. (I should add a vertical line at the  $k$  of the coarse mesh for visualization purposes.)

### 5.2 Mesh force at grid distances

The actual force of gravity in the  $P^3M$  algorithm, as felt by a single particle, is presented in the left panel of Fig. 5. The left panel shows the force versus distance – in fine cell units – a calculation that was performed from a CITA256 realization in two steps: 1- we compute the force on each particle in a given time step. 2- we remove a selected particle, compute the force again on all particles, and record on file the force difference (before and after the removal) as a function of the distance to the ‘hole’.

Particles in the same fine cell as the hole follow the exact  $1/r^2$  curve. The scatter at distances of the order of the fine grid is caused by the NGP interpolation scheme: particles in adjacent fine cells can be actually very close, as seen in the upper left region of this plot, but still feel the mesh force at grid cell distances, creating up to an order of magnitude loss. As the separation approaches a tenth of the full box size or so, the force on the coarse mesh deviates from Newton's law in order to preserve periodic boundary conditions. This feature, however, can be turned off at compilation time.

The right panel of Fig. 5 shows the fractional error on the force along the radial and tangential directions, calculated from a single time step. It is larger than in PMFAST at grid scales, largely due to the fact that the fine mesh force is performed with an NGP interpolation scheme – as opposed to CIC – which shows a larger scatter about the theoretical value. This change of interpolation is essential for the pp part.

The biggest problem with the straightforward pp force calculation is that the results are anisotropic and depend on the location

of the fine mesh with respect to the particles. As an example, consider two particles on either side of a grid cell boundary, experiencing their mutual gravity attraction via the fine mesh force with a discretized 1-grid cell separation. If, instead, the mesh was shifted such that they were within the same cell, they would experience the much larger pp force. This effect is especially pronounced at the early stages of the simulation where the density is more homogeneous, and leads to mesh artefacts appearing in the density field. In order to minimize this systematic effect, we randomly shift the particle distribution relative to the mesh by a small amount – up to 2 fine grid cells in magnitude – in each dimension and at each time step. This adds negligible computational overhead as it is applied during the particle position update, and suppresses the mesh behaviour that otherwise grows over multiple time steps. It is possible to shift back the particles at the end of each time steps, which prevents a random drift of the whole population, a necessary step if one needs to correlate the initial and final positions of the particles for instance, or for hybrid dark matter – MHD simulations.

We ensure that, on average, this solution balances out the mesh feature, by tuning the force kernels such as to provide force as evenly balanced as possible at grid cell distances and at the cut-off length ( $r_c = 16$  fine cells). These adjustments are performed from a pairwise force test described in MPT. We note that this is one of the driving argument to extend the pp force outside the fine mesh cell, since the scattering of the NGP force about the actual  $1/r^2$  law drops rapidly as the distance increases. As discussed in section 7.3, this gain in accuracy comes at a price, a choice that must be carefully balanced.

We present in Fig. 6 the dramatic impact of removing the random offset in the code. The power spectrum is completely wrong, due to the large scatter in the force from the fine mesh. In this scatter is not averaged over, the error directly adds up at each time step. PMFAST did not have this problem since it used CIC interpolation on both meshes. This test was performed with CITA256 simulations of very large box size, which should in principle agree with linear predictions up to the resolution. The output redshifts are very early, and the upper most curve ( $z = 10$ ) was obtained after about 60 time steps. We see that deviations are enormous when the random offset is turned off.

To illustrate how well the random offset performs, we present in Fig. 7 the impact of averaging over 10 time steps. We recast the same force test in which we dig a hole, with the addition that we apply a random offset the whole particle population at the end of the calculation. We repeat this operation ten times, always extracting the same particle, and average the mean force and the deviation. When compared with a single time step, we see that the scatter has reduced by almost a factor of three in the radial direction, while the transverse deviation shows a milder improvement.

### 5.3 Constraining redshift jumps

At early stages of the simulation, the density fields is rather homogenous, causing the force of gravity to be rather weak everywhere. In that case, the size of the redshift jumps is controlled by a limit in the cosmological expansion. If the expansion jump is too large, the size of the residual errors can become significant, and one can observe, for instance, a growth of structure that does not match the predictions of linear theory even at the largest scales. One therefore needs to choose a maximum step size. In CUBEP3M, this is controlled by  $r_{max}$ , which is the fractional step size,  $da/(a+da)$  and is set to 0.05 by default. Generally, a simulation should start at a redshift high enough that the initial dimensionless power spectrum

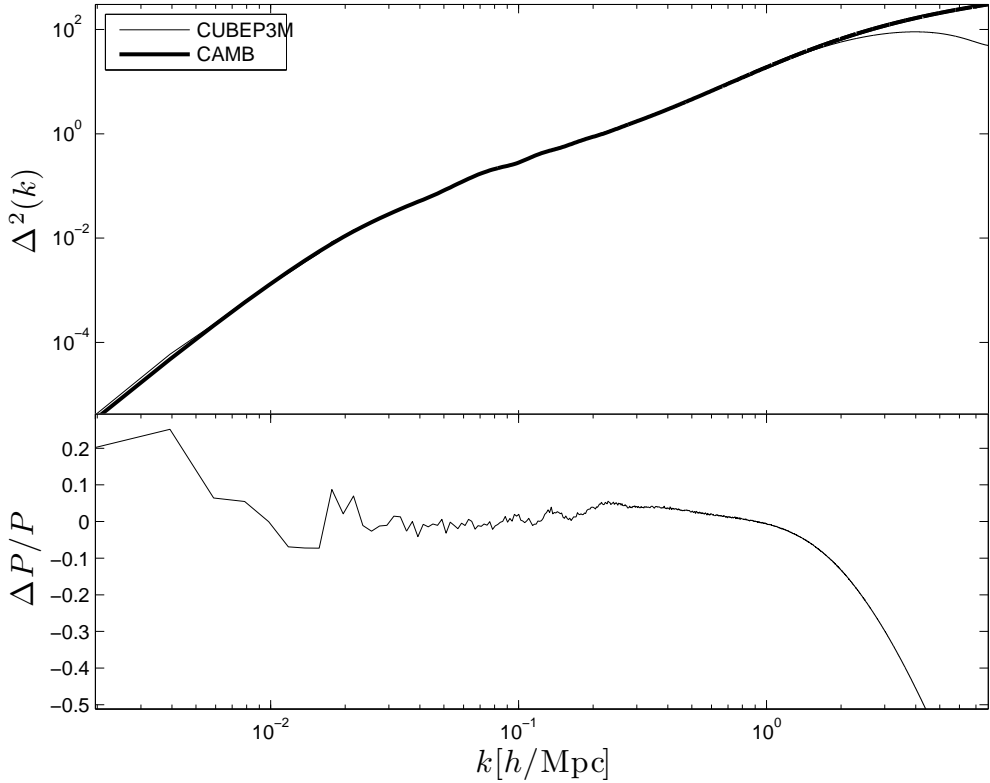


**Figure 4.** Dark matter power spectrum, measured at  $z = 0$  in a RANGER4000 simulation, compared to the non-linear predictions of CAMB.

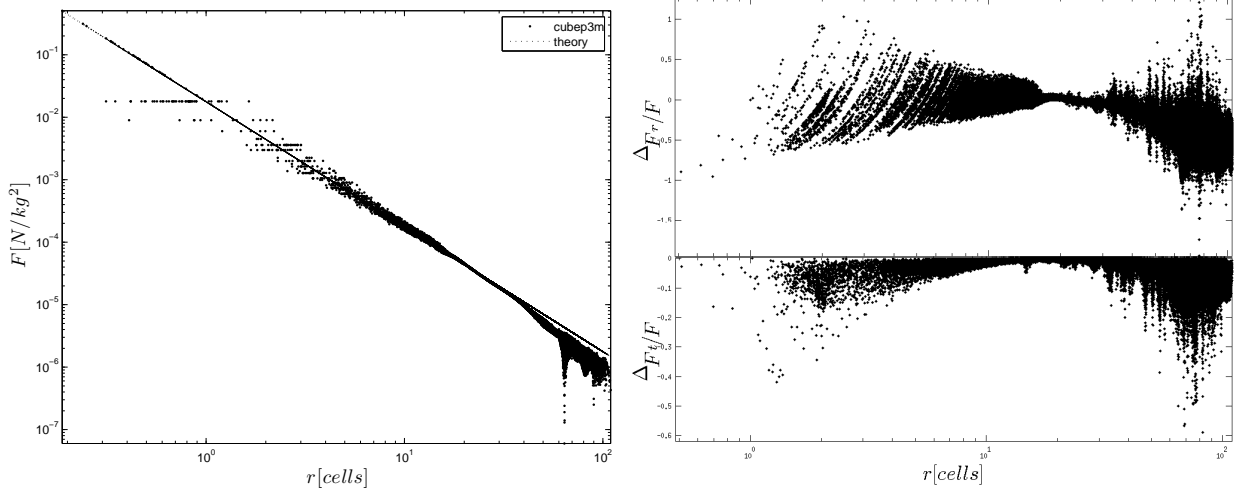


**Figure 5.** (left:) Gravity force in of the P<sup>3</sup>M algorithm, versus distance in fine mesh cell units, compared with the exact  $1/r^2$  law. This particular calculation was obtained in a CITA256 realization with a box size of  $500h^{-1}\text{Mpc}$ , in a single time step. (right:) Fractional error on the force in of the P<sup>3</sup>M algorithm, in the radial (top) and tangential (bottom) directions. In a full simulation run, the scatter averages over many time steps, thanks to the inclusion of a random offset that is imposed on each particle, as discussed in the main text.

is well under unity at all scales. This ensures that the Zel'dovich approximation holds at the per cent level at least. A drop of accuracy can occur if one starts the simulation too early, where truncation error will be significant at the early time steps.

It is possible to reduce this effect, and thereby improve significantly the accuracy of the code, by modifying the value of  $r_{max}$ , at the cost of increasing the total number of time steps. Fig. 8 shows

a comparison of late time power spectra of a series of CITA256 realizations that originate from the same initial conditions, and used the same random seeds to control the fine mesh shifts (mentioned above): only the value of  $r_{max}$  was modified between each run. We observe that the impact is mostly located in the non-linear regime, where decreasing the time step to 0.006 allows the simulation to recover about 30 per cent of dimensionless power at the turn over

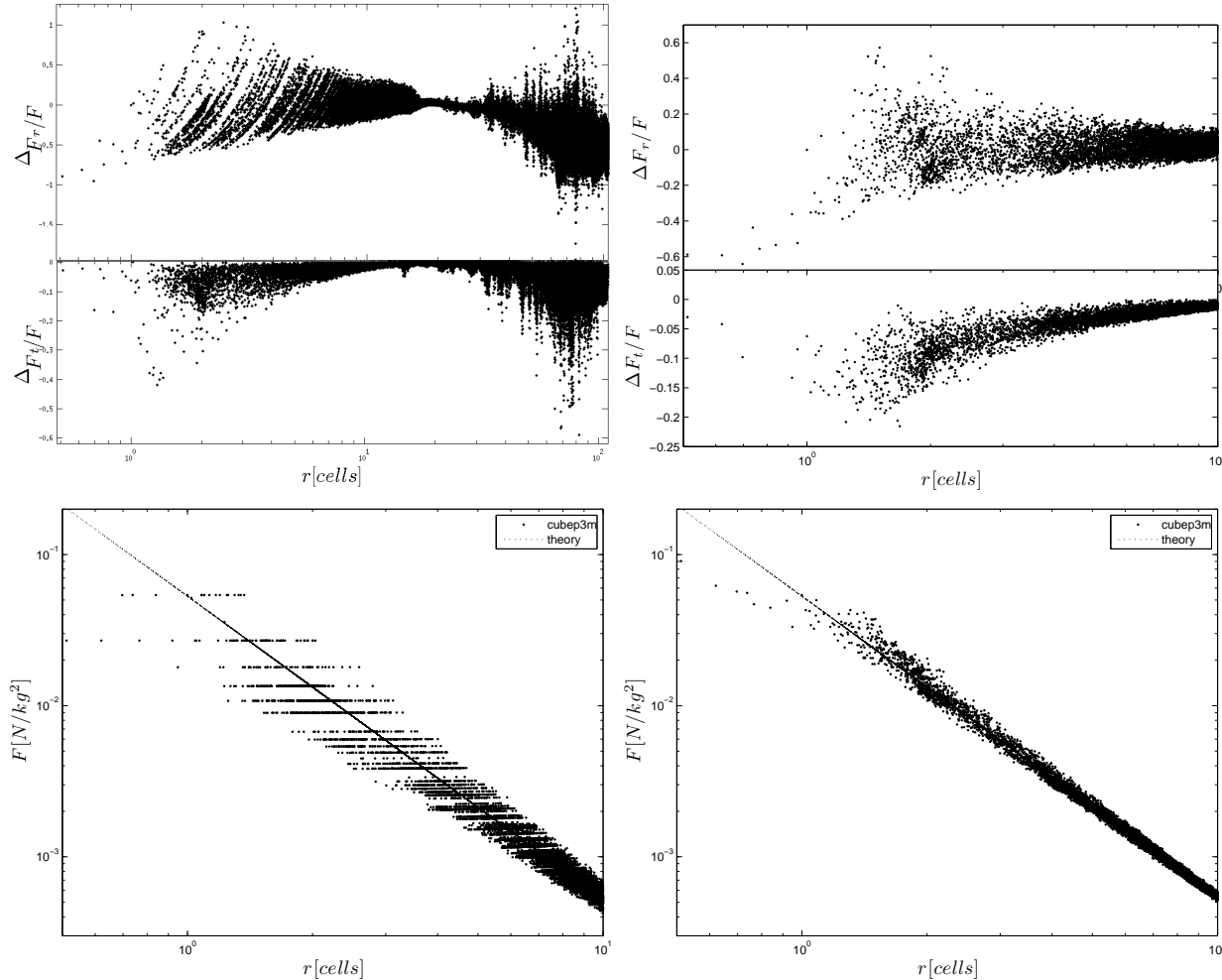


**Figure 7.** (top:) Gravity force in of the  $P^3M$  algorithm, versus distance in fine mesh cell units, compared with the exact  $1/r^2$  law. This particular calculation was obtained in a CITA128 realization with a box size of  $100h^{-1}\text{Mpc}$ . (bottom:) Fractional error on the force in of the  $P^3M$  algorithm, in the radial (top) and tangential (bottom) directions. The left panels are calculated from a single time step, while the right panels show the average over time steps.

scale, in this simulation configuration. This gain is greatly affected by the choice of initial redshift, the resolution, and the box size, and ideally one would make test runs in order to optimize a given configuration. As expected, the CPU resources required to run these simulations increase rapidly as  $r_{max}$  decreases, as seen in Table 3. In this test case, reducing further at 0.001 shows only a mild improvement in accuracy, but the increase in time is more than a factor of four. We should mention that with a proper use of the non-Gaussian initial conditions, it is possible to start the simulations at much later redshifts, where the time step sizes are dominated by a stronger mesh force.

#### (Any other systematics effects we want to discuss here?)

## 6 RUNTIME HALO FINDER

We have implemented a halo finding procedure, which we have developed based on the spherical overdensity (SO) approach (Lacey & Cole 1994). In the interest of speed and efficiency the halo catalogues are constructed on-the-fly at a pre-determined list of redshifts. The halo finding is massively-parallel and threaded based on the main CUBEP3M data structures discussed in section 2. The

**Table 3.** Scaling in CPU resources as a function of the value of  $r_{max}$ . The tests were performed on the CITA Sunnyvale cluster, and general trends could vary slightly on other machines.

$r_{max}$	time (h)
0.1	1.46
0.06	1.48
0.01	1.67
0.006	1.91
0.003	2.83
0.002	4.13
0.001	8.15

code first builds the fine-mesh density for each sub-domain using CIC or NGP interpolation. It then proceeds to search for and record all local density maxima above certain threshold (typically set to 100 above mean density) within the local sub-domain's physical volume (excluding the sub-domain buffer zones). It then uses parabolic interpolation on the density field to determine more precisely the location of the maximum within the densest cell, and records the peak position and value. The halo centre determined

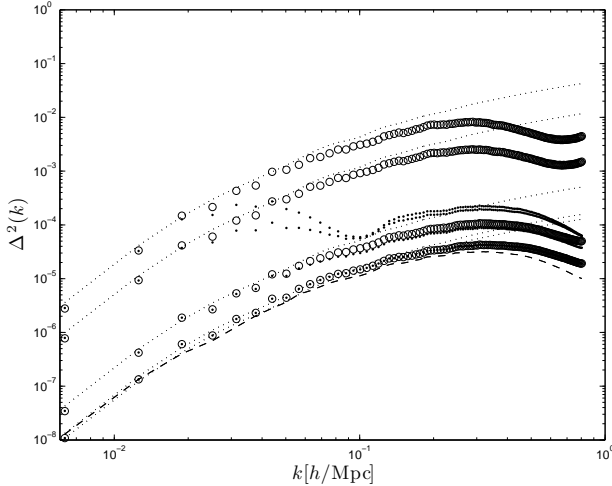


**Figure 6.** Dark matter power spectrum, measured at  $z = 180, 100, 20$  and  $10$ , in a series of CITA256 realizations that are  $1000 \text{ Mpc}/h$  per side. The dashed line represent the initial condition power spectrum, the dotted lines are the linear predictions, and the open circles the standard  $P^3M$  configuration. The dots were obtained by simply removing the random particle offset that is usually applied at each time step.

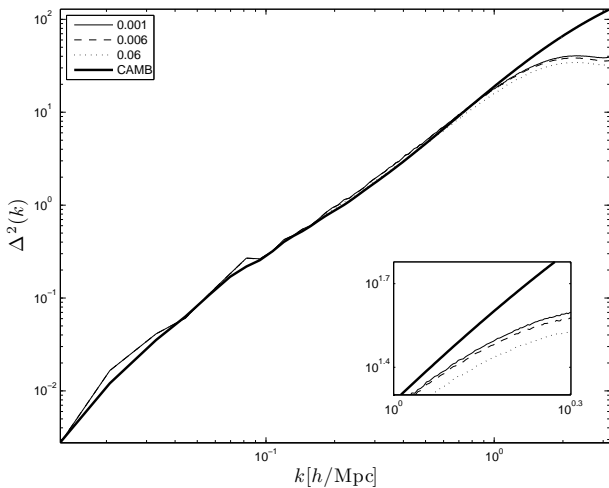


**Figure 8.** Dark matter power spectrum, measured at  $z = 0$  in a series of CITA256 realizations. The starting redshift of was raised to  $z = 200$  to enhance the systematic effect. The different curves show different values of  $r_{\max}$ . The resources required to run these simulations increase rapidly as  $r_{\max}$  decreases, as seen in Table 3.

this way agrees closely with the centre-of-mass of the halo particles discussed below.

Once the list of peak positions is generated, they are sorted from the highest to the lowest density value. Then each of the halo candidates is inspected independently, starting with the highest peak. The grid mass is accumulated in spherical shells of fine grid cells surrounding the maximum, until the mean density within the halo drops below a pre-defined overdensity cutoff (usually set to 178 in units of the mean, in accordance to the top-hat collapse model). As we accumulate mass we remove it from the mesh, so that no mass element is double-counted. This method is thus inappropriate for finding sub-halos as within this framework those are naturally incorporated in their host halos. Because the halos are

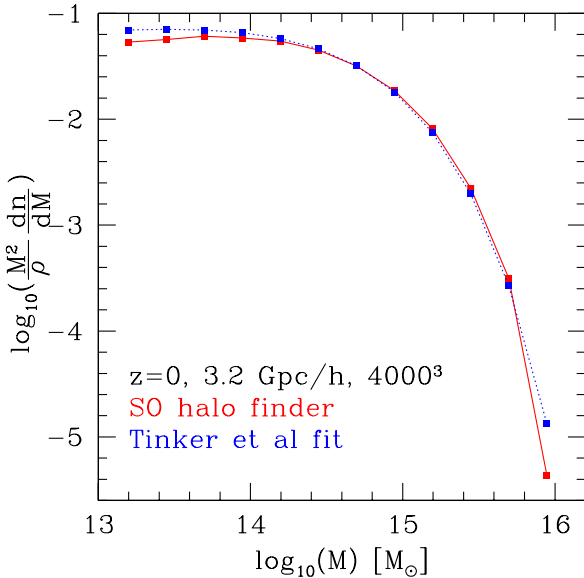


**Figure 9.** Simulated halo multiplicity function,  $\frac{M^2}{\rho} \frac{dn}{dM}$  based on a RANGER4000 simulation with  $3.2 h^{-1} \text{Gpc}$  box and  $4000^3$  particles (solid, red in the online version). For reference we also show a widely-used precise fit by Tinker et al. (2008) (blue, dashed).

found on a grid of finite-size cells, it is possible, especially for the low-mass halos, to overshoot the target overdensity. When this occurs we use an analytical halo density profile to correct the halo mass and radius to the values corresponding to the target overdensity. This analytical density profile is given by Truncated Isothermal Sphere (TIS) profile (Shapiro et al. 1999; Iliev & Shapiro 2001) for overdensities below  $\sim 130$ , and  $1/r^2$  for lower overdensities. The density profile has a similar outer slope (the relevant one here) to the Navarro, Frenk and White (NFW Navarro et al. 1997) profile, but extends to lower overdensities and matches well the virialization shock position given by the Bertschinger self-similar collapse solution (Bertschinger 1985).

Once the correct halo mass, radius and position are determined, we find all particles which are within the halo radius. Their positions and velocities are used to calculate the halo centre-of-mass, bulk velocity, internal velocity dispersion and the three angular momentum components, all of which are then included in the final halo catalogues. We also calculate the total mass of all particles within the halo radius, also listed in the halo data. This mass is very close, but typically slightly lower, than the halo mass calculated based on the gridded density field. The particle centre-of-mass corresponds very well to the halo centre found based on the gridded mass distribution.

A sample halo mass function produced based on our inlined SO halo finder at redshift  $z = 0$  from a RANGER4000 simulation is shown in Fig. 9. We compare our result to the precise fit presented recently by Tinker et al. (2008). Unlike most other widely-used fits like the one by Sheth & Tormen (2002), which are based on friends-of-friends (FOF) halo finders, the Tinker et al. (2008) fit is based on the SO search algorithm, whose masses are systematically different from the FOF masses (e.g. Reed et al. 2007; Tinker et al. 2008), making this fit a better base for comparison here. Results show excellent agreement, within  $\sim 10$  per cent for all halos with masses corresponding to 1000 particles or more. Lower-mass halos

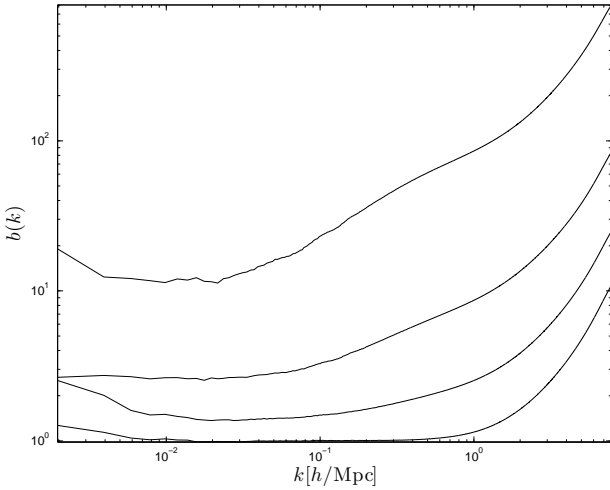


**Figure 10.** Halo bias, measured at  $z = 0$  from a RANGER4000 simulation with a side length of  $3.2h^{-1}\text{Gpc}$ . Bottom to top curves correspond to haloes of different masses, from light to massive. The four bins are decades of halo masses; the first contains haloes made of 20–200 particles, the second of 200–2,000 and so on.

are somewhat under-counted compared to the Tinker et al. (2008) fit, by  $\sim 20$  per cent for 400 particles and by  $\sim 40$  per cent for 50 particles. This is due to the grid-based nature of our SO halo finder, which misses some of the low-mass halos. It was shown, however, that using more sophisticated halo finders (available through post-processing due to their heavier memory footprint) allows to recover the expected mass function.

A second test of the accuracy of the halo finder algorithm is to extract the halo power spectrum  $P_h(k)$  and compare the halo bias with theoretical predictions. The halo bias is defined as  $b(k) = \sqrt{P(k)/P_h(k)}$  and is shown in Fig. 10. **Expand here, describe, match with theory, etc...**

## 7 BEYOND THE STANDARD CONFIGURATION

The preceding descriptions and discussions apply to the standard configuration of the code, as described at the beginning of section 2. A few extensions have been recently developed in order to enlarge the range of applications of CUBEP3M, and this section briefly describe the most important improvements.

### 7.1 Initial Conditions

As mentioned in section 2, the code starts off by reading a set of initial conditions. These are organized as a set of  $6 \times N$  phase-space arrays – one per MPI process – where  $N$  is the number of particles in the local volume. Although many applications are typically based on initial conditions that follow Gaussian statistics, we have developed a non-Gaussian initial conditions generator that we briefly describe in this section.

The original code that provides Gaussian initial conditions for CUBEP3M is extended to include non-Gaussian features of the ‘local’ form,  $\Phi(\mathbf{x}) = \phi(\mathbf{x}) + f_{NL}\phi(\mathbf{x})^2 + g_{NL}\phi(\mathbf{x})^3$ , where  $\phi(\mathbf{x})$  is the Gaussian contribution to the Bardeen potential  $\Phi(\mathbf{x})$  (see Bartolo et al. (2004) for a review). We adopted the CMB convention, in which  $\Phi$  is calculated immediately after the matter–radiation equality (and not at redshift  $z = 0$  as in the large scale structure conven-

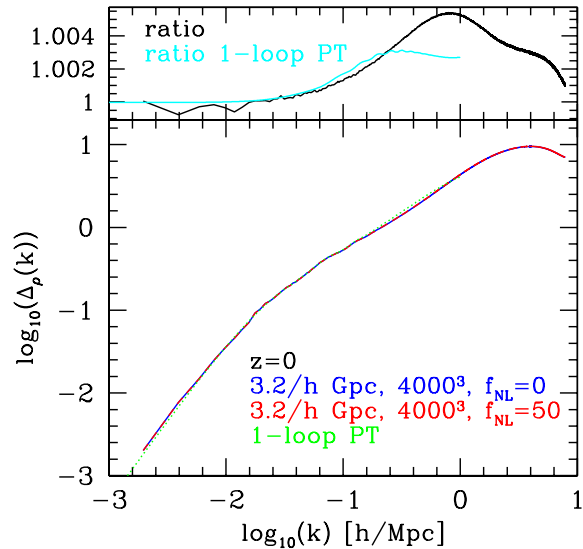


**Figure 11.** Dark matter power spectrum, measured at  $z = 0$  in a volume  $3.2h^{-1}\text{Gpc}$  per side, from  $4000^3$  particles. The two curves represent two RANGER4000 realizations of the same initial power spectrum, one of which used Gaussian statistics (blue) and the other the non-Gaussian initial condition generator. The two curves differ at the sub-per cent level, as seen in the top panel, and the non-Gaussian realization is in much better agreement with the one-loop perturbation theory calculations.

tion). For consistency,  $\phi(\mathbf{x})$  is normalized to the amplitude of scalar perturbations inferred by CMB measurements ( $A_s \approx 2.2 \times 10^{-9}$ ). The local transformation is performed before the inclusion of the matter transfer function, and the initial particle positions and velocities are finally computed from  $\Phi(\mathbf{x})$  according to the Zel’dovich approximation, as in the original Gaussian initial condition generator.

This code was tested by comparing simulations and theoretical predictions for the effect of local primordial non-Gaussianity on the halo mass function and matter power spectrum (Desjacques, Seljak & Iliev 2009). It has also been used to quantify the impact of local non-Gaussian initial conditions on the halo power spectrum (Desjacques et al. 2009; Desjacques & Seljak 2010) and bispectrum (Sefusatti et al. 2010), as well as the matter bispectrum (Sefusatti et al. 2011). Fig. 11 shows the late time power spectrum of two RANGER4000 realizations that started off the same initial power spectrum, but one of which had non-Gaussian initial conditions. We see that the difference between the two power spectra is at the sub-per cent level, but that the non-Gaussian realization agrees much better with one loop perturbation theory (Scoccimarro et al. 2004; Taruya et al. 2008).

### 7.2 Particle identification tags

A system of particle identification can be turned on, which basically allows to track each particle’s trajectory between checkpoints. Such a tool is useful for a number of applications, from reconstruction of halo merging history to tracking individual particle trajectories. The particle tag system has been implemented as an array of double integers, PID, and assigns a unique integer to each particle during the initialization stage. The location of the tag on the PID array matches the location of the corresponding particle on the xv array,

hence it acts as if the latter array had an extra dimension. The location change only when particles exist the local volume, in which case the tag is sent along adjacent nodes with the particle in the `pass_particle` subroutine, and deleted particles result in deleted flags. Similarly to the phase space array, the PID array gets written to file at each particle checkpoint. Since the array takes a significant amount of memory, we opted to store the tags in a separate object – as opposed to adding an extra dimension to the existing `xv` array, such that it can be turned off when memory becomes an issue.

### 7.3 Extended range of the pp force

One of the main source of error in the calculation of the force occurs when on the smallest scales of the fine grid. The approximation by which particles in a neighbouring mesh grid can be placed at the centre of the cell is less accurate, which cause a maximal scatter around the exact  $1/r^2$  law. A solution to minimize this error consists in extending the pp force calculation outside a single cell, which inevitably reintroduces a  $N^2$  number of operations. Our goal is to add the flexibility to have a code that runs slower, but produces results with a higher precision.

To allow this feature, we have to choose how far outside a cell we want the exact pp force. Since the force kernels on both meshes are organized in terms of grids, the simplest way to implement this feature is to shut down the mesh kernels in a region of specified size, and allow the pp force to extend therein. Concretely, these regions are constructed as cubic layers of fine mesh grids around a central cell; the freedom we have is to choose the number of such layers.

To speed up the access to all particles within the domain of computation, we construct a thread safe linked list to be constructed and accessed in parallel by each core of the system, but this time with a head-of-chain that points to the first particle in the current fine mesh cell. We then loop over all fine grids, accessing the particles contained therein and inside each fine grid cells for which we killed the mesh kernels, we compute the separation and the force between each pairs and update their velocities simultaneously with Newton's third law. To avoid double counting, we loop only over the fine mesh neighbours that produce non-redundant contributions. Namely, for a central cell located at  $(x_1, y_1, z_1)$ , we only consider the neighbours  $(x_2, y_2, z_2)$  that satisfy the following conditions:

- $z_2 \geq z_1$  always
- if  $z_2 = z_1$ , then  $y_2 \geq y_1$ , otherwise we also allow  $y_2 < y_1$
- if  $z_2 = z_1$  and  $y_2 = y_1$ , then we enforce  $x_2 > x_1$

The case where all three coordinates are equal is already calculated in the standard configuration of the code. To assess the improvement of the force calculation, we present in Fig 12 a force versus distance plot in a CITA256 realization, analogous to Fig. 5, but the pp force has been extended to six layers of fine cells. We observe that the scatter about the theoretical curve has reduced significantly, and is still well balanced around the theoretical predictions. The same applies to the fractional error on the radial and tangential components of the force, as seen in Fig. 13, which are now at least 5 time smaller than in the default P<sup>3</sup>M algorithm.

To quantify the accuracy improvement versus computing time requirements, we performed the following test. We generate a set of initial conditions at a starting redshift of  $z = 100$ , with a box size equal to  $200h^{-1}\text{Mpc}$ , and with  $256^3$  particles. We evolve these CITA256 realizations with different ranges for the pp calculation, and compare the resulting power spectra. For the results to be

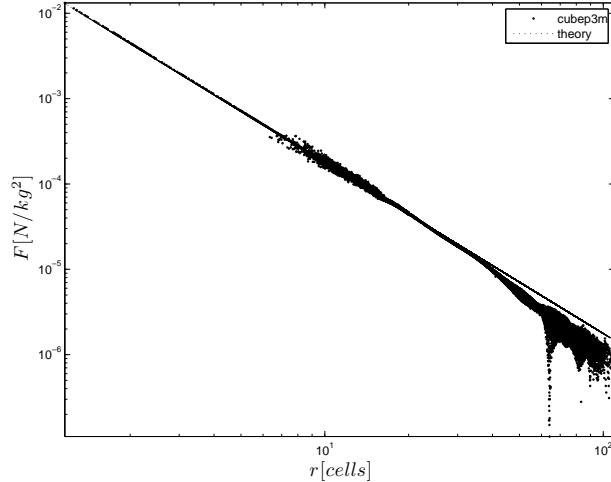


**Figure 12.** Gravity force in the P<sup>3</sup>M algorithm, compared with the exact  $1/r^2$  law, in a CITA256 realization. The exact pp force has been extended to six fine mesh layers around each particle. Particles in the that range follow the exact curve, then we observe a much smaller scatter at distance of the order of 6 fine grid, compared to Fig. 5. The NGP interpolation scheme is again responsible for the scatter, but the effect is suppressed with increasing distances, and further suppressed by averaging over many time steps..

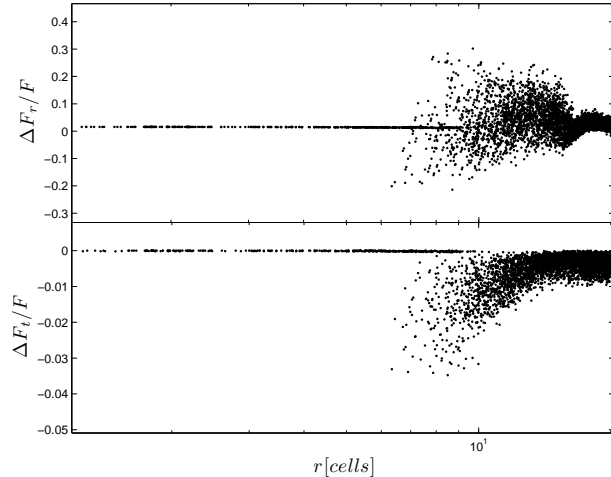


**Figure 13.** Fractional error on the force in the P<sup>3</sup>M algorithm, in the radial (top) and tangential (bottom) directions, in a CITA256 simulation in which the exact pp force extends to six fine mesh layers. This was obtained over a single time step.

meaningful, we also need to use the same random seed for the random number generator, such that the only difference between different runs is the range of the pp force. Fig. 14 shows the dimensionless power spectrum of the different runs, where we see a significant gains in resolution when extending PM to P<sup>3</sup>M first, and when adding successive layers of fine cell mesh where the pp force is extended. We have not plotted the results for higher numbers of layers, as the improvement becomes milder there: the fine grid calculations are more accurate as the distance increases. For this reason, it seems that a range of a few layers, between 3 and 6, suffices to reduce most of the undesired NGP scatter.

Extending the pp calculation comes at a price, since the number of operation scales as  $N^2$  in the sub-domain. This cost is best capture by the increase of real time required by a fixed number of

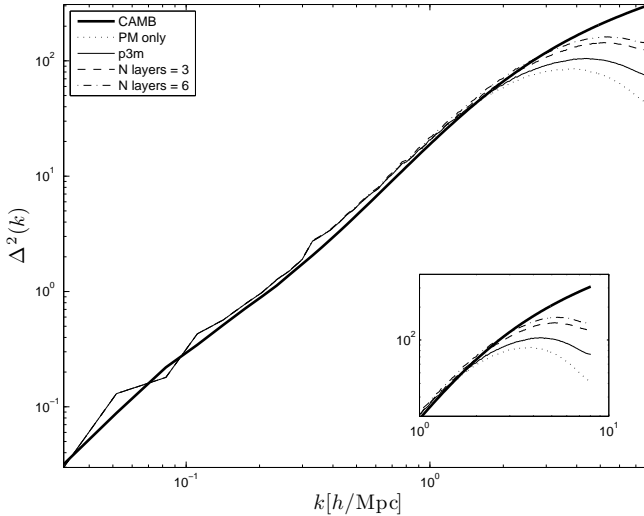


**Figure 14.** Dimensionless power spectrum for varying range of the exact pp force, compared to CAMB (Lewis et al. 2000). These CITA256 realizations evolved from a unique set of initial conditions at a starting redshift of  $z = 100$ , with a box size equal to  $200/h^{-1}$  Mpc until  $z = 0$ . The only difference between the runs is the ranges of the pp calculation.

**Table 4.** Scaling in CPU resources as a function of the range of the pp interaction.  $N_{layers}$  refers to the number of fine mesh layers around a given cell, inside of which the force calculation is purely given by the pp contribution.

Type	time (h)
PM	1.77
$P^3M$	2.09
<hr/>	
$N_{layers}$	
1	8.74
2	11.47
3	14.30
4	18.87
5	22.52
6	29.62
7	34.82
8	47.00

dedicated CPUs to evolved the particles to the final redshift. Table 4 presents this usage.

Perhaps the most relevant way to quantify the improvement of the calculation is to measure the impact on the halo mass function from these different CITA256 runs. Fig. 15 presents this comparison at redshift zero. About 11,000 haloes were found in the end, and we observe a good match with the Sheth-Tormen predictions.

## 8 CONCLUSION

This paper describes CUBEP3M, a public  $P^3M$  N-body code that is massively parallel, memory local, and that scales well to 20,000 cores, thus raising the limits of the cosmological problem size one can handle. We summarize the code structure, the two-mesh Poisson solver algorithm, we present scaling and systematic tests that have been performed. We also describe a few utilities and exten-

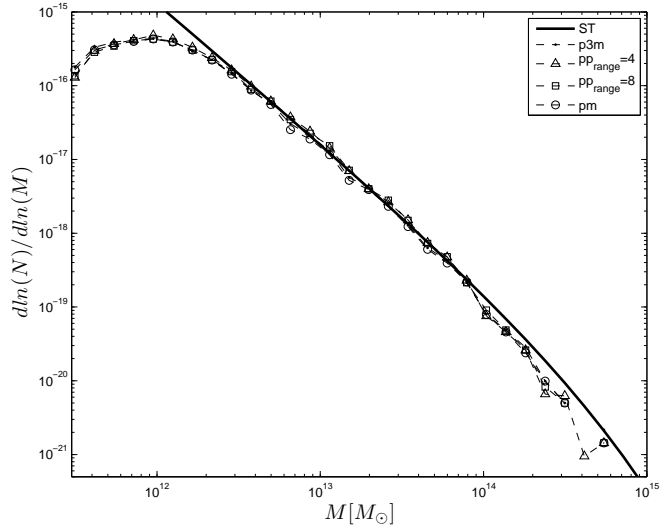


**Figure 15.** Halo mass function for different ranges of the pp force calculation, compared to the predictions of Sheth-Tormen. (y-axis?)

sions that come with the public release, including a run time halo finder, an extended pp force calculation and a non-Gaussian initial condition generator.

The code is publicly available on [github.com](http://github.com) under `cubep3m`, and extra documentation about the structure, compiling and running strategy is can be found at [www.wiki.cita.utoronto.ca/mediawiki/index.php/CubePM](http://www.wiki.cita.utoronto.ca/mediawiki/index.php/CubePM).

## ACKNOWLEDGEMENTS

The CITA256 simulations were run on the Sunnyvale cluster at CITA. ITI was supported by The Southeast Physics Network (SEPNet) and the Science and Technology Facilities Council grants ST/F002858/1 and ST/I000976/1. The authors acknowledge the TeraGrid and the Texas Advanced Computing Center (TACC) at The University of Texas at Austin (URL: <http://www.tacc.utexas.edu>) for providing HPC and visualization resources that have contributed to the research results reported within this paper. ITI also acknowledges the Partnership for Advanced Computing in Europe (PRACE) grant 2010PA0442 which supported the code scaling studies.

## REFERENCES

- Eleftheriou M., Fitch B. G., Rayshubskiy A., Ward T. J. C., Germain R. S., 2005, IBM J. Res. Dev., 49, 457
- Bartolo N., Komatsu E., Matarrese S., Riotto A., 2004, Phys. Rep., 402, 103
- Bertschinger E., 1985, ApJS, 58, 39
- Colless M., et al., 2003, ArXiv e-prints (astro-ph/0306581)
- Couchman H. M. P., 1991, ApJ, 368, L23
- Couchman H. M. P., Thomas P. A., Pearce F. R., 1995, ApJ, 452, 797
- Datta K. K., Mellema G., Mao Y., Iliev I. T., Shapiro P. R., et al., 2011, arXiv:1109.1284
- Desjacques V., Seljak U., 2010, Phys. Rev. D, 81, 023006
- Desjacques V., Seljak U., Iliev I. T., 2009, MNRAS, 396, 85

- Doré O., Lu T., Pen U.-L., 2009, ArXiv e-prints
- Drinkwater M. J., et al., 2010, MNRAS, 401, 1429
- Dubinski J., Kim J., Park C., Humble R., 2004, NewA, 9, 111
- Eisenstein D. J., et al., 2005, ApJ, 633, 560
- Fernandez E. R., Iliev I. T., Komatsu E., Shapiro P. R., 2011, arXiv:1112.2064
- Friedrich M. M., Datta K. K., Mellema G., Iliev I. T., 2012, ArXiv e-prints
- Friedrich M. M., Mellema G., Alvarez M. A., Shapiro P. R., Iliev I. T., 2011, MNRAS, 413, 1353
- Frigo M., Johnson S., 2005, in Proceedings of the IEEE Vol. 93, The Design and Implementation of FFTW3. pp 216–231
- Harnois-Déraps J., Pen U.-L., 2011, ArXiv e-prints
- Harnois-Déraps J., Vafaei S., Van Waerbeke L., 2012, ArXiv e-prints
- Harnois-Déraps J., Yu H.-R., Zhang T.-J., Pen U.-L., 2012, ArXiv e-prints
- Heymans C., CFHTLenS Collaboration 2012, in American Astronomical Society Meeting Abstracts Vol. 219 of American Astronomical Society Meeting Abstracts, The CFHT Lensing Survey. p. 130.01
- Hilbert S., Hartlap J., White S. D. M., Schneider P., 2009, A&A, 499, 31
- Hockney R. W., Eastwood J. W., 1981, Computer Simulation Using Particles
- Iliev I. T., Freese K., Valluri M., Iliev I. T., Shapiro P. R., 2012, MNRAS, p. 2794
- Iliev I. T., Ahn K., Koda J., Shapiro P. R., Pen U.-L., 2010, proceedings paper for Moriond 2010 meeting (ArXiv:1005.2502)
- Iliev I. T., Mellema G., Pen U.-L., Merz H., Shapiro P. R., Alvarez M. A., 2006, MNRAS, 369, 1625
- Iliev I. T., Mellema G., Shapiro P. R., Pen U.-L., Mao Y., Koda J., Ahn K., 2011, ArXiv e-prints
- Iliev I. T., Shapiro P. R., 2001, MNRAS, 325, 468
- Iliev I. T., Shapiro P. R., Mellema G., Merz H., Pen U.-L., 2008, in refereed proceedings of TeraGrid08, ArXiv e-prints (0806.2887)
- Komatsu E., Dunkley J., Nolta M. R., Bennett C. L., Gold B., Hinshaw G., Jarosik N., Larson D., Limon M., Page L., Spergel D. N., Halpern M., Hill R. S., Kogut A., Meyer S. S., Tucker G. S., Weiland J. L., Wollack E., Wright E. L., 2009, ApJS, 180, 330
- Komatsu E., et al., 2011, ApJS, 192, 18
- Lacey C., Cole S., 1994, MNRAS, 271, 676
- Lewis A., Challinor A., Lasenby A., 2000, Astrophys. J., 538, 473
- Lu T., Pen U.-L., 2008, MNRAS, 388, 1819
- Lu T., Pen U.-L., Doré O., 2010, Phys. Rev. D, 81, 123015
- Mao Y., Shapiro P. R., Mellema G., Iliev I. T., Koda J., Ahn K., 2012, MNRAS, 422, 926
- Mellema G., Iliev I. T., Alvarez M. A., Shapiro P. R., 2006, New Astronomy, 11, 374
- Merz H., Pen U.-L., Trac H., 2005, New Astronomy, 10, 393
- Navarro J. F., Frenk C. S., White S. D. M., 1997, ApJ, 490, 493
- Ngan W.-H. W., Harnois-Déraps J., Pen U.-L., McDonald P., MacDonald I., 2011, ArXiv e-prints (astro-ph/1106.5548)
- Percival W. J., Cole S., Eisenstein D. J., Nichol R. C., Peacock J. A., Pope A. C., Szalay A. S., 2007, MNRAS, 381, 1053
- Reed D. S., Bower R., Frenk C. S., Jenkins A., Theuns T., 2007, MNRAS, 374, 2
- Rimes C. D., Hamilton A. J. S., 2005, MNRAS, 360, L82
- Sato M., Hamana T., Takahashi R., Takada M., Yoshida N., Matsubara T., Sugiyama N., 2009, ApJ, 701, 945
- Schlegel D., White M., Eisenstein D., 2009, ArXiv e-prints (astro-ph/0902.4680)
- Scoccimarro R., Sefusatti E., Zaldarriaga M., 2004, Phys. Rev. D, 69, 103513
- Sefusatti E., Crocce M., Desjacques V., 2010, MNRAS, 406, 1014
- Sefusatti E., Crocce M., Desjacques V., 2011, ArXiv e-prints
- Shapiro P. R., Iliev I. T., Raga A. C., 1999, MNRAS, 307, 203
- Sheldon E. S., Johnston D. E., Masjedi M., McKay T. A., Blanton M. R., Scranton R., Wechsler R. H., Koester B. P., Hansen S. M., Frieman J. A., Annis J., 2009, ApJ, 703, 2232
- Sheth R. K., Tormen G., 2002, MNRAS, 329, 61
- Springel V., 2005, MNRAS, 364, 1105
- Springel V., Yoshida N., White S. D. M., 2001, New Astronomy, 6, 79
- Takahashi R., et al., 2009, ApJ, 700, 479
- Takahashi R., et al., 2011, ApJ, 726, 7
- Taruya A., Koyama K., Matsubara T., 2008, Phys. Rev. D, 78, 123534
- Tegmark M., et al., 2006, Phys. Rev. D, 74, 123507
- Tinker J., Kravtsov A. V., Klypin A., Abazajian K., Warren M., Yepes G., Gottlöber S., Holz D. E., 2008, ApJ, 688, 709
- Trac H., Cen R., 2007, ApJ, 671, 1
- Trac H., Pen U., 2003, in American Astronomical Society Meeting Abstracts Vol. 35 of Bulletin of the American Astronomical Society, Out-of-Core Hydrodynamic Simulations of the IGM. p. 1365
- Trac H., Pen U.-L., 2004, NewA, 9, 443
- Vafaei S., Lu T., van Waerbeke L., Sembolini E., Heymans C., Pen U.-L., 2010, Astroparticle Physics, 32, 340
- Vale C., White M., 2003, ApJ, 592, 699
- Xu G., 1995, ApJS, 98, 355
- York D. G., et al., 2000, AJ, 120, 1579
- Yu H., Zhang T., Harnois-Déraps J., Pen U., 2010, ArXiv e-prints
- Zackrisson E., Scott P., Rydberg C.-E., Iocco F., Sivertsson S., Östlin G., Mellema G., Iliev I. T., Shapiro P. R., 2010, MNRAS, 407, L74
- Zahn O., Lidz A., McQuinn M., Dutta S., Hernquist L., Zaldarriaga M., Furlanetto S. R., 2007, ApJ, 654, 12
- Zhang T., Yu H., Harnois-Déraps J., MacDonald I., Pen U., 2010, ArXiv e-prints

This paper has been typeset from a  $\text{\TeX}$ /  $\text{\LaTeX}$  file prepared by the author.